Nuclear Materials and Energy 22 (2020) 100732

Contents lists available at ScienceDirect

Nuclear Materials and Energy

journal homepage: www.elsevier.com/locate/nme

HRXRD study of the theoretical densities of novel reactive sintered boride candidate neutron shielding materials

J.M. Marshall*, D. Walker, P.A. Thomas

Department of Physics, University of Warwick, Gibbet Hill Road, Coventry CV4 7AL, UK

ARTICLE INFO

Keywords:
Radiation shielding
Nuclear fusion
Tungsten borides
Cemented carbides
XRD
Powder metallurgy

ABSTRACT

Reactive Sintered Borides (RSBs) are novel borocarbide materials derived from FeCr-based cemented tungsten (FeCr-cWCs) show considerable promise as compact radiation armour for proposed spherical tokamak (Humphry-Baker, 2007 [1], [2], [3], [4], [5]. Six candidate compositions (four RSBs, two cWCs) were evaluated by high-resolution X-ray diffraction (XRD), inductively coupled plasma (ICP), energy dispersive X-ray analysis (EDX) and scanning electron microscopy (SEM) to determine the atomic composition, phase presence, and theoretical density.

RSB compositions were evaluated with initial boron contents equivalent to 25 at% $< x <$ 40 at%. Stable RSB bodies formed from sintering for compositions where B at% > 30 at%. All RSB compositions showed delamination and carbon enrichment in the bulk relative to the surface, consistent with non-optimal binder removal and insufficient sintering time. Phase abundance within RSBs derived from powder XRD was dominated by iron tungsten borides ($FeWB/FeW_2B_2$), tungsten borides (W_2B_5/WB) and iron borides. The most optimal RSB composition (B5T522W) with respect to physical properties and highest ρ/ρ_{theo} had $\rho_{theo} = 12.59 \pm 0.01$ g cm^{-3} for $\rho/\rho_{theo} = 99.3\%$ and had the weigh-in and post-sintered W: B: Fe abundance closest to 1: 1: 1. This work indicates that despite their novelty, RSB materials can be optimized and in principle be processed using existing cWC processing routes.

1. Introduction

Nuclear fusion is at a critical point where power-generating reactors are feasible within the next decade, following recent advances with compact fusion devices worldwide [6]. The recent demonstration of high magnetic field controlled fusion within a compact spherical tokamak (cST), using high-temperature superconducting (HTS) magnets has shown that fusion conditions can be achieved in compact devices [7]. A significant factor limiting the further development of compact fusion reactors is that current candidate materials do not meet the engineering requirements within a power generating cST reactor. In particular, the central column of a cST that receives the most intense neutron and gamma radiation [3,4], alongside the thermal load and represents the greatest materials challenge.

Candidate shielding materials must fulfil generic materials challenges and radiological safety requirements. These include (but not limited to) (1) thermal expansion, (2) heat resistance and (3) the extreme temperature gradient between the plasma-facing component of the first wall (plasma temperature~10^8 K) to the cryogenic HTS at the core. HTS magnets are also highly sensitive to ionizing radiation [8,9]. Current shielding solutions based on refractory metals and W-based alloys as the most favoured candidates [10,11], however the engineering requirements for power-generating fusion reactors still exceed the properties of current candidate materials [10]. In addition to the requirements listed above, shielding must also be able to satisfy regulatory requirements in the case of accidents. This is a particular issue for W-alloy based shields since W oxidizes rapidly at $T > 900$ °C [12]. Previous studies [2,3,13] on cemented Tungsten Carbide (cWCs) and have identified W–B–C–Fe–Cr-based Reactive Sintered Borides (RSBs) as a potential candidate for enhancing neutron-absorbing refractory shielding materials.

Until recently, cWCs had received little attention as radiation shielding materials since the most common ductile binder alloys are based on Co and Ni, both activation hazards under irradiation. The binary FeCr (8 wt% Cr, Fe–8Cr) alloy was identified as a suitable a Co-substitute in 2014 [14] for a ductile cWC metallic binder [1,15] and is compatible with existing powder metallurgy (PM) processing. Since neither Fe or Cr activate significantly under neutron or gamma irradiation, the use of Fe-8Cr enables the use of cWCs in radioactive environments for the first time. Simulations of combined neutron and

* Corresponding author.
E-mail addresses: j.marshall.4@warwick.ac.uk (J.M. Marshall), david.walker.2@warwick.ac.uk (D. Walker), p.a.thomas@warwick.ac.uk (P.A. Thomas).

https://doi.org/10.1016/j.nme.2020.100732
Received 19 November 2019; Received in revised form 28 January 2020; Accepted 28 January 2020
Available online 04 February 2020

gamma irradiation on a combined cWC-RSB shield outperformed metallic tungsten for certain configurations [4,13,16]. Further investigations using silicide coatings have also demonstrated significant advantages of cWCs over W metal in terms of high-temperature oxidization resistance [5,17], critical for accident tolerance in the worst-case scenario of hot shielding exposed to air following a loss of coolant accident.

RSB synthesis followed on from boron additions in FeCr-cWCs when it was observed that mixtures of B_4C (4 wt% $< x <$ 9 wt%), Fe-8Cr (21 wt% $< x <$ 25 wt%) and W metal to balance also formed dense sintered bodies [14] using the same PM route as for cWCs. RSBs are potentially excellent neutron attenuators, but data on their physical properties is lacking due to their novelty [2,14]. Prior research on similar refractory borides (W, Mo, Re, etc.) has focused on their properties as ultra-hard or magnetic materials rather than as candidate nuclear shielding solutions [18].

The first quantitative investigation of phase presence in RSBs by high-resolution XRD (HRXRD) is reported in this study. Theoretical densities from HRXRD data were calculated for each RSB composition, enabling evaluation of the true sintered density and porosity for the first time.

2. Method

Samples of cWC and RSB materials were produced by laboratory-scale PM processing [1,19,20]. FeCr-cWC-based controls, referred to as JBTE10 and B1TE10 used WC powder with target d_{WC} = 0.8 μm (Wolfram Bergbau) and pre-alloyed Cr–Fe steel powder (Osprey). RSBs consisted of B_4C (Alpha Aesar), Fe–8Cr and W metal (Wolfram Bergbau) powder to balance to form a 100 g powder charge. No carbon was added to cWC mills as is the general case for cWCs [1,19,20] to establish a baseline sintered cWC composition. Weigh-in quantities are shown in Table 1:

Nomenclature depends on reagent weigh-in as seen in Table 1. The cWC sample is referred to as JBTEx, where x denotes the wt% of the Fe–8Cr alloy on weigh-in. For boron- containing materials, the following convention BxTEy(W) is used, where x = weigh-in wt% of B_4C, y = Fe–8Cr wt% at weigh-in, and W for W metal powder additions to balance. Powder charges were milled as for general cWCs [2,19,20], with a 2 wt% addition of polyethylene glycol (PEG) based organic binder additive as a pressing aid. Post milling, powders were dried, sieved and uniaxially pressed into a variety of geometries, including cutting tools (green dimensions 25 × 8 × 6 mm), square cuboid (green dimensions 20 × 20 × 8 mm) and wear test plates (green dimensions 50 × 30 × 6 mm). Cutting tool and cuboid geometries were uniaxially pressed between 50 and 100 MPa and wear plate samples pressed at 25 MPa. Green samples were treated using a standard cWC de-binding cycle to remove the PEG prior to SinterHIPPing. Samples were sinter-HIPPed in an Ar atmosphere at 50 bar in graphite crucibles lined with alumina felt with a 1 h hot dwell at 1450 °C. Post sintering, samples were evaluated using cWC quality control methods [1,19,20]. Mechanical hardness was evaluated using a Vickers diamond indenter with a 30 kg equivalent load on polished cross-sectioned samples of cutting tool geometry only. The critical stress intensity factor ($K1_c$) was evaluated from the resulting Palmqvist cracks using the Shetty method [19]. Density was measured using the Archimedes method with a modified Precisa 125 balance with an uncertainty of ± 0.1 mg.

Table 1
Weigh-in compositions for cWC and RSB samples. A cWC-RSB sample is any sample with boron and WC present at weigh-in.

Composition Weigh-in	wt% WC	Fe-8Cr	B_4C	W	Material Type
JBTE10	90	10	0	0	cWC
B1TE10	89	10	1	0	cWC-RSB
B4TE21W	0	21	4	75	RSB
B5T522W	0	22	5.5	72.5	RSB
B7TE23W	0	23	7	70	RSB
B9TE25W	0	25	9	66	RSB

Sample microstructure was assessed by scanning electron microscopy (SEM) with a Zeiss SUPRA 55VP system, energy dispersive X-ray analysis (EDX) using Oxford Instruments INCA EDX system, and X-ray diffraction (XRD). Inductively coupled plasma (ICP) analysis (Exeter Analytical) was performed on powder samples to determine elemental abundances to an accuracy of 0.1 at%. ICP analysis was used as a standard to correct EDX analysis used for compositional analysis on sample surface and cross-sections and to set limits for XRD models.

HRXRD analysis on bulk and powder samples was performed using a Phillips PANalytical Empyrean diffractometer running at 40 mA at 40 kV, using Co radiation (λ = 1.78 Å) to mitigate Fe-based fluorescence. Samples were cut using a cubic boron nitride (cBN) wheel (Agar Scientific) with a South Bay Technologies cutter. Solid samples were sequentially polished with SiC paper and diamond polish down to 1 μm then annealed in air at 150–250 °C for 1 h. Powder samples were pulverized in an iron percussion mortar and sieved to < 75 μm. XRD samples were scanned for 15 h and 3 h for powder and solid samples, respectively. Initial phase identification was performed using PANalytical High Score Plus to determine suitable PDF files for structure models.

Reitveld refinement was performed using TOPAS Academic 6. Restraints for XRD models in TOPAS were determined from ICP-EDX derived elemental abundance to ensure that models were compatible with measured atomic abundances and densities. Due to the large number of phases used in each model, refinements were limited to lattice parameters, atomic positions and isotropic thermal parameters. Quality of XRD models was assessed from the Bragg factor weighted profile R-factor (R_{wp}) and the goodness-of-fit (GoF) [21,22].

3. Results

3.1. Physical properties of sintered samples

Sintered cWC and RSB samples are shown in Fig 1.

Baseline cWC-based samples JBTE10 and B1TE10 showed no significant porosity or delamination features on cutting and polishing, despite being carbon deficient. All RSB samples showed gross linear features on cross-sectional cutting, most notably in Fig. 1(c) and (d), indicative of delamination during the PEG removal part of the sintering cycle. Some distortion was observed from sintered RSB samples, most notably compositions B4TE21W and B7TE23W on the wear plate samples. A critical part of cWC PM processing is ensuring that the decomposition of the PEG organic binder is controlled such that reaction products are removed at a suitable rate during the de-binding stage of sintering, since PEG decomposition is autocatalytic and exothermic. Non-optimal PEG removal results in porosity and delamination [23] as seen in Fig. 1(d). Physical properties and Archimedes densities of sintered samples are shown in Table 2. In contrast, composition B5T522W showed no obvious distortion as shown in Fig. 1(b) with a few gross delamination features on cross-sectioning. From Fig. 1(c) widespread delamination and fractures were observed for composition B4TE21W. Physical properties and Archimedes densities of sintered samples are shown in Table 2.

The values of shrinkage and mass loss for RSB materials were consistent with those from cWCs [1,19] which have three-dimensional shrinkages between 16 and 22% depending on target d_{WC} and metallic binder content [18,20,24]. Mass-loss was between 2 and 3%, attributable to a net carbon loss and PEG de-binding during sintering. Shrinkage and mass-loss for RSBs indicate that these materials are compatible with existing PM processing methods. Hardness and toughness values from the cWC-based controls are consistent with values from fine-grained cWCs (target sintered d_{WC} < 1.0 μm) [20,24].

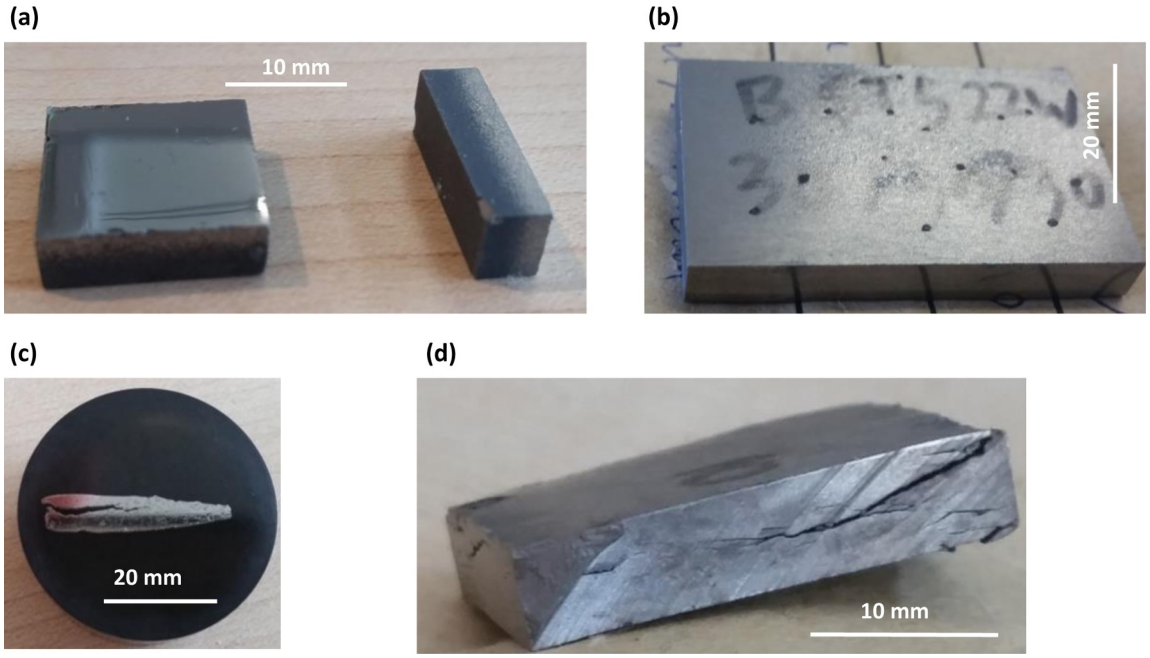

Fig. 1. Sintered cWC and boride samples. a shows unmodified cWC (JBTE10) polished for XRD and as-sintered, b as-sintered wear test plate of RSB B5T522W, c polished cross-section of wear test sample RSB B4TE21W and d cross-section of as-sintered RSB B9TE25W. Delamination and splitting are present for both c B4TE21W and d B9TE25W.

Table 2
Shrinkage, mass-loss, mechanical properties in sintered materials.

Compositions	Shrinkage %	Mass loss %	HV30 kgf mm^{-2}	K_{1c} MPa m$^{0.5}$
JBTE10	17.91	2.18	1764	7.3
B1TE10	15.89	2.91	1826	7.2
B4TE21W	16.51	3.10	1369	6.5
B5T522W	22.03	2.98	1505	8.4
B7TE23W	18.27	3.30	1319	6.3
B9TE25W	19.59	3.02	1072	6.3

For RSBs, hardness is generally lower than cWCs, as is toughness but comparable with some TiC-enriched cermets [25]. However, values of hardness and toughness for RSBs were obtained from cutting tool samples only, while those from the cWC samples are from a selection of geometries – these values are representative of a small volume fraction within RSBs relative to cWCs due to their non-optimized processing status.

3.2. Sample composition

Phase presence must be consistent with the elemental abundance of the sintered body. Atomic abundances calculated from (a) reagent weigh-in and (b) sintered compositions measured by combined ICP-EDX analysis are shown in Fig. 2.

Atomic abundances for the cWC samples show carbon loss consistent with standard cWC PM processing [19,20]. Carbon loss was more variable for RSBs, consistent with non-optimal PEG removal for RSBs relative to cWCs. RSBs loss much more carbon relative to cWCs during sintering, with composition B7TE23W having the largest net carbon loss and B5T522W losing the least carbon during sintering. Composition B5T522W showed little carbon loss with 7.7 at% from reagents to 7.4 at% post sintering in this study. Prior work by Windsor et al. [2] measured sintered carbon content equivalent to 5.6 at% for the same composition, so it is probable that this disparity results from sampling effects and compositional inhomogeneity within RSBs. It is well known in cWC PM processing that non-optimal PEG removal can lead to excess carbon within cWCs [23,26], relative to optimized debinding cycles as seen in Fig. 1. Boron content also showed some change post sintering relative to weigh-in. Composition B4TE21W showed little change to boron abundance post sintering. Compositions B5T522W, B7TE23W and B9TE25W appeared to shift closer to atomic ratios based on W: Fe: B ≈ 1: 1: 1 at% ratio post-sintering, relative to atomic abundance calculated from reagent weigh-in quantities. This is particularly noticeable for composition B9TE25W with respect to shifts in B and W content pre- and post-sintering in Fig. 2(a) and (e).

3.3. Sample microstructure

The SE images from cWC-based samples JBTE10 and B1TE10 are shown in Fig. 2.

Considerable intermetallic carbide formation ($M_{12}C/M_{23}C_6$, M = W, Fe, Cr), indicative of carbon deficient cWCs [2,18,20] is observed for JBTE10 (Fig. 3(a)) as predicted without carbon additions. Fig. 3(a) shows $d_{WC} < 0.8$ μm, consistent with the inhibition of Ostwald ripening from the carbon-deficient FeCr binder [1,16,27]. B1TE10 (Fig. 3(b)) shows a much reduced $M_{12}C$ presence relative to JBTE10 (Fig. 3(a)). Reduction in $M_{12}C$ presence is consistent with the carbon from B_4C, with the needle-like morphology seen alongside ternary phase presence in Fig. 3(b) resulting from probable WB/W_2B_5 formation.

All samples showed well-defined regions of W-rich lighter Z-contrast with smaller regions of dark Fe(Cr)-B enriched Z-contrast surrounded by regions of mixed phases, although for composition B4TE21W the light and dark contrast regions are irregular. Crystals and regions of well-defined Z-contrast are visible in for compositions B5T522W-B9TE25W in Fig. 3(d)–(f). All RSB compositions show most porosity near interfaces between high/low Z contrast and grain boundaries. Two compositions, B5T522W and B9TE25W (Fig. 3(d) and (f)) have a highly complex phase field with mixed tungsten and iron borides present and long WB-rich crystals dominating the microstructure. In contrast, B7TE23W (Fig. 3(e)) shows a quasi-binary phase-field dominated by large W-rich crystals and FeB/Fe_2B in the interstices. Scalloped features on the surface of grains are indicative of brittle fracture during polishing in Fig. 3(e) with similar features present for B9TE25W. This is

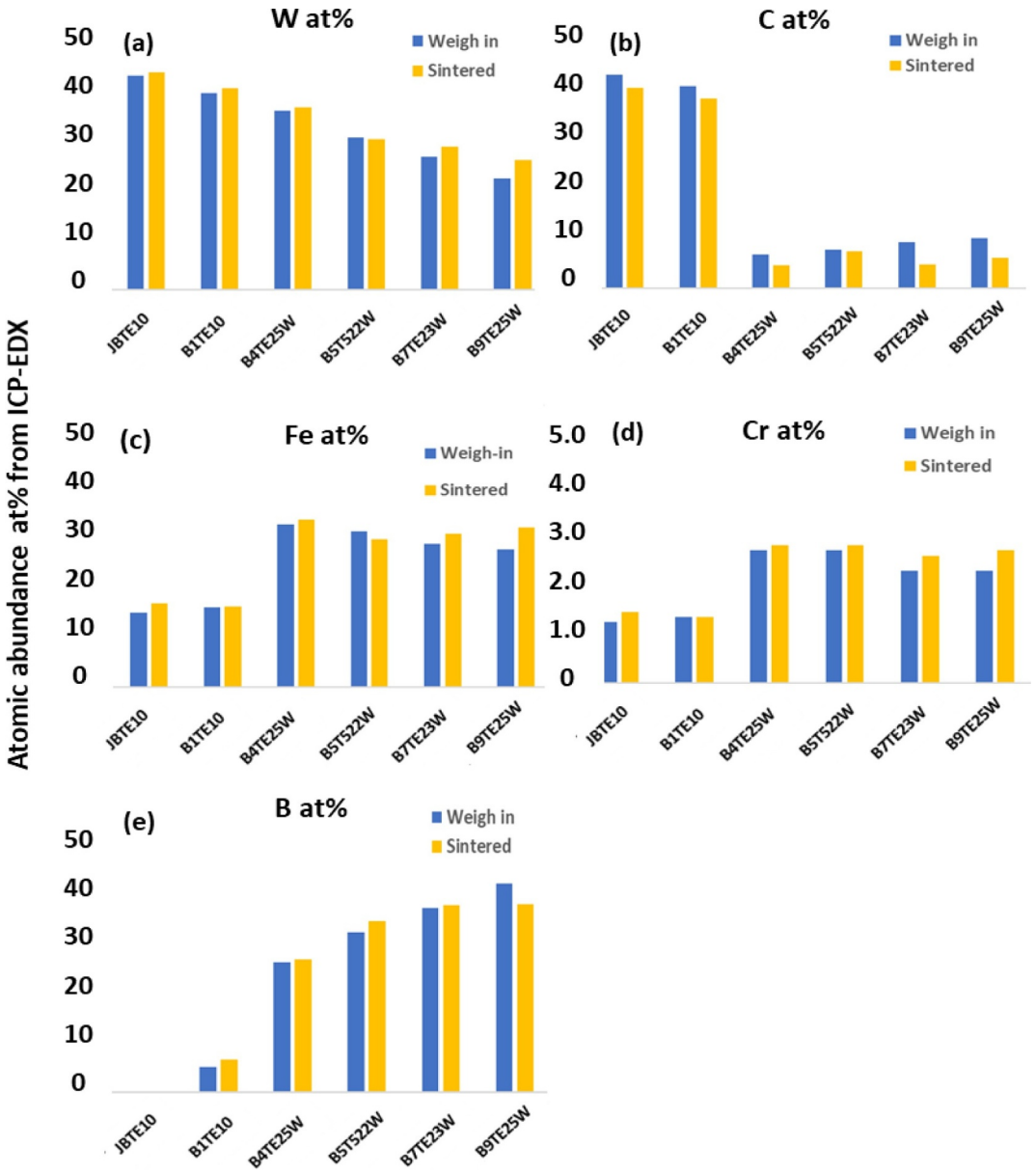

Fig. 2. Atomic abundances calculated from reagents and sintered materials for each species. (a) W at%, (b) C at%, (c) Fe at%, (d) Cr at% and (e) B at%.

reflected in the lower fracture toughness and hardness for B7TE23W and B9TE25W relative to B5T522W as seen in Section 3.1.

3.4. HRXRD – quantitative phase abundance

HRXRD diffraction patterns were obtained from powder and polished surfaces from all cWC and RSB samples. The lack of a broad peak at low 2θ indicative of amorphous content was absent for all spectra, indicating phases present are highly crystalline. Constraints on phase abundance within were set by the atomic abundances measured from ICP and EDX analysis from powder samples in Fig. 2 were applied as restraints to TOPAS models, using the assumption that the powder phase presence is more representative of the whole sample than the surface phases. From 30+ trial phases, a total of 21 phases were indexed for all cWC-RSBs examined in this study. Similarly, only the powder difference ($Y_{calc,\ powder} - Y_{obs,\ powder}$) is shown since the powder difference represents all the indexed phases and is always greater than the solid difference. Spectra from cWC and RSB powder samples are shown in Fig. 4.

No significant differences between powder and solid samples were observed for either cWC-based samples JBTE10 and B1TE10. JBTE10 shows a significant ternary phase presence ($M_{12}C$) as predicted from carbon loss during sintering [1,19] and in Fig. 3(a), Section 3.2. B1TE10 showed no detectable $M_{12}C$ presence but small peaks indicative of trace W_2B_5 and Fe_2B presence were detected, consistent with the microstructural features shown in Fig. 3(b). Spectra from RSB samples (Fig. 4(c)–(f)) are indicative of a complex phase field with > 90% of the diffracted intensity is accounted for by 7–8 dominant phases for all RSB compositions. All RSB samples show peaks attributable to FeWB/FeW_2B_2, WB/W_2B_5, and FeB_2/FeB, with specific intensities differing with RSB composition. Composition B4TE21W shows significant peaks attributable to W_2B and W_2C in the powder spectra and Fe_7W_6/Fe_2W in the solid spectra respectively in Fig. 4(c). Composition B5T522W is dominated by reflections attributed to FeWB/FeW_2B_2, WB/W_2B_5 and FeB/Fe_2B with WC reflections in the solid samples in Fig. 4(d). B7TE23W is an outlier in that its phase field is dominated by FeWB/FeW_2B_2 and iron borides, consistent with the microstructure shown in Fig. 3(e). Spectra from B5T522W and B9TE25W have superficial similarities in terms that both have strong WB/W_2B_5 and FeB/Fe_2B peaks and significant WC presence, with B9TE25W shows more peaks

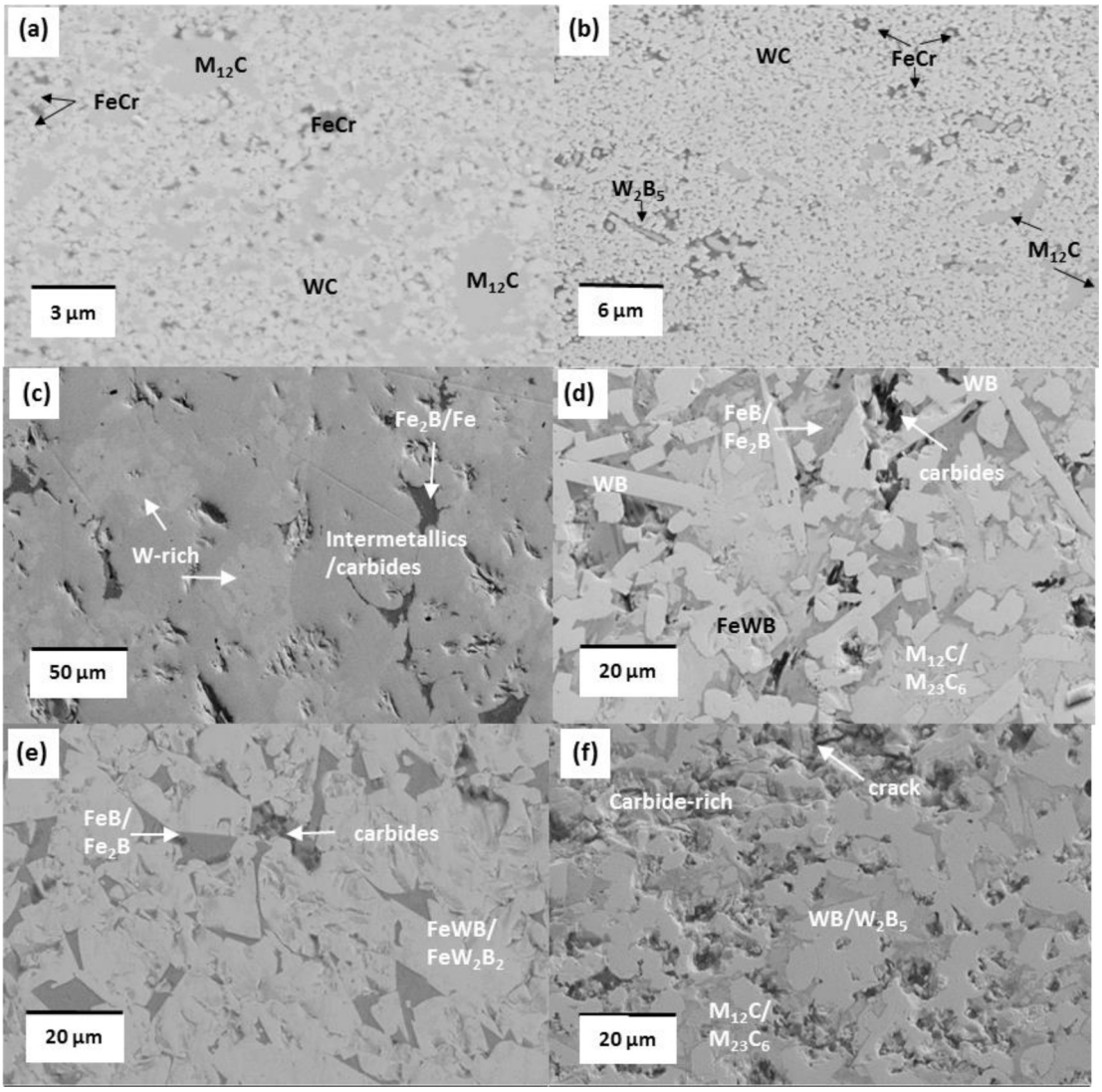

Fig. 3. SE image for cWC-based samples a Unmodified FeCr-cWC JBTE10 and b 1 wt% B_4C-doped cWC B1TE10. WC phase is the lightest (high Z) contrast with FeCr binder as dark low-Z contrast. $M_{12}C$ is visible as intermediate contrast in (a) and (b). RSB compositions in (c) B4TE21W, (d) B5T522W, (e) B7TE23W and f B9TE23W listed in order of ascending boron content. Long WB-rich crystals dominate the structures seen in d, e and f as mid-range contrast, darker contrast mostly consist of FeB/Fe_2B.

attributable to lower-mass carbides (Cr_xC_y/Fe_3C).

For all RSB samples, >90% of all diffracted intensity was attributed to 7 categories. These are: a FeWB/FeW_2B_2, b Fe_2B/FeB, c WB/W_2B_5, d WC, e Fe_7W_6/Fe_2W, f $M_{12}C$/$M_{23}C_6$ and g tungsten-rich phases W_2C/W_2B. Minor diffracting phases include simple carbide/borides, e.g. CrB, WB_4 for instance and can be seen in the supplementary data. No intensity was attributed to mixed (W, Cr)B or any mixed (Fe,W,Cr) borocarbides but this does not prove their absence. X-ray models from TOPAS indicate that Cr and Fe segregate and form discrete borides, not (Fe, Cr)B or (Fe, Cr)(B, C) and that Cr preferentially segregates to the $M_{12}C$/$M_{23}C_6$ carbides, not Fe_xW_yZ borides. RSBs show a wide disparity in phase presence but the sintered compositions of B7TE23W and B9TE25W in Fig. 2, Section 3.2 are similar in atomic composition, with carbon content having the greatest difference between these two compositions. The differences in microstructures between B7TE23W and B9TE25W appears to have a stronger correlation between sintered carbon content than weigh-in compositions. It is probable that for RSB weigh-in compositions where W ≈ Fe ≈ B at%, the rate of carbon depletion and hence net carbon content has a more significant impact on sintered microstructure than the initial W: Fe(Cr): B weigh-composition suggests.

3.5. XRD: bulk and surface compositions

No significant difference between surface and powder spectra was observed from cWCs samples, consistent with a sintering process optimized for cWCs. Assuming that powder samples are representative of bulk compositions, surface spectra from RSBs generally showed phases more consistent with carbon-deficient compositions, including W_2C/W_2B, FeB/Fe_2B, and Fe_7W_6/Fe_2W, relative to powder spectra from all compositions. Composition B7TE23W (Fig. 4(e)) shows the least variation between bulk and surface spectra but does show more WC and mixed $M_{12}C$/$M_{23}C_6$ presence from the powder relative to the surface, indicative of a more carbon-rich interior relative to the surface. Variations between powder and surface phase composition in terms of the seven phase categories defined in Section 3.4 for RSB compositions are shown in Fig. 5.

Phase abundances determined from both powder and surface spectra were consistent with observed sintered composition, with B4TE21W having the highest concentration of Fe_xW_y, $M_{12}C$/$M_{23}C_6$ and W-rich phases (W_2C and W_2B) and B9TE25W being dominated by WB/W_2B_5 borides. When microstructure is considered alongside phase content, Figs. 3 and 5 show some evidence that higher carbon content

(B5T522W and B9TE25W) enhances the growth of WB/W_2B_5 relative to compositions with lower carbon content (B7TE23W), which are more $FeWB/FeW_2B_2$ dominated.

3.6. Composition: EDX-ICP measurements and XRD models

Bragg factors are an indicator of how the calculated intensity (Y_{calc}) fits the observed diffracted intensity (Y_{obs}), where R_{wp} is the weighted profile *R*-factor and R_{exp} is the Bragg factor predicted for a perfect model where $Y_{calc}–Y_{obs} = 0$ [21,22] and is dependent on the total number of counts. The goodness-of-fit (GoF) can be derived from R_{WP}/R_{exp} [21,22]. Restrictions on each phase entered in the model were determined both by measured atomic abundance and R_{WP} within the final model. XRD models where the phase abundance and the resulting atomic composition most closely matched the ICP-EDX derived atomic abundance generally converged to the lowest R_{WP} factors. The Bragg Factors of the most optimal cWC-RSB models are shown in Table 3.

The low R_{exp} results in part from the high value of *N* and the high count-rate from the spectra and since R_{exp} is proportional to $1/\sqrt{N}$ [21], where *N* is the total number of counts within an XRD diffraction pattern

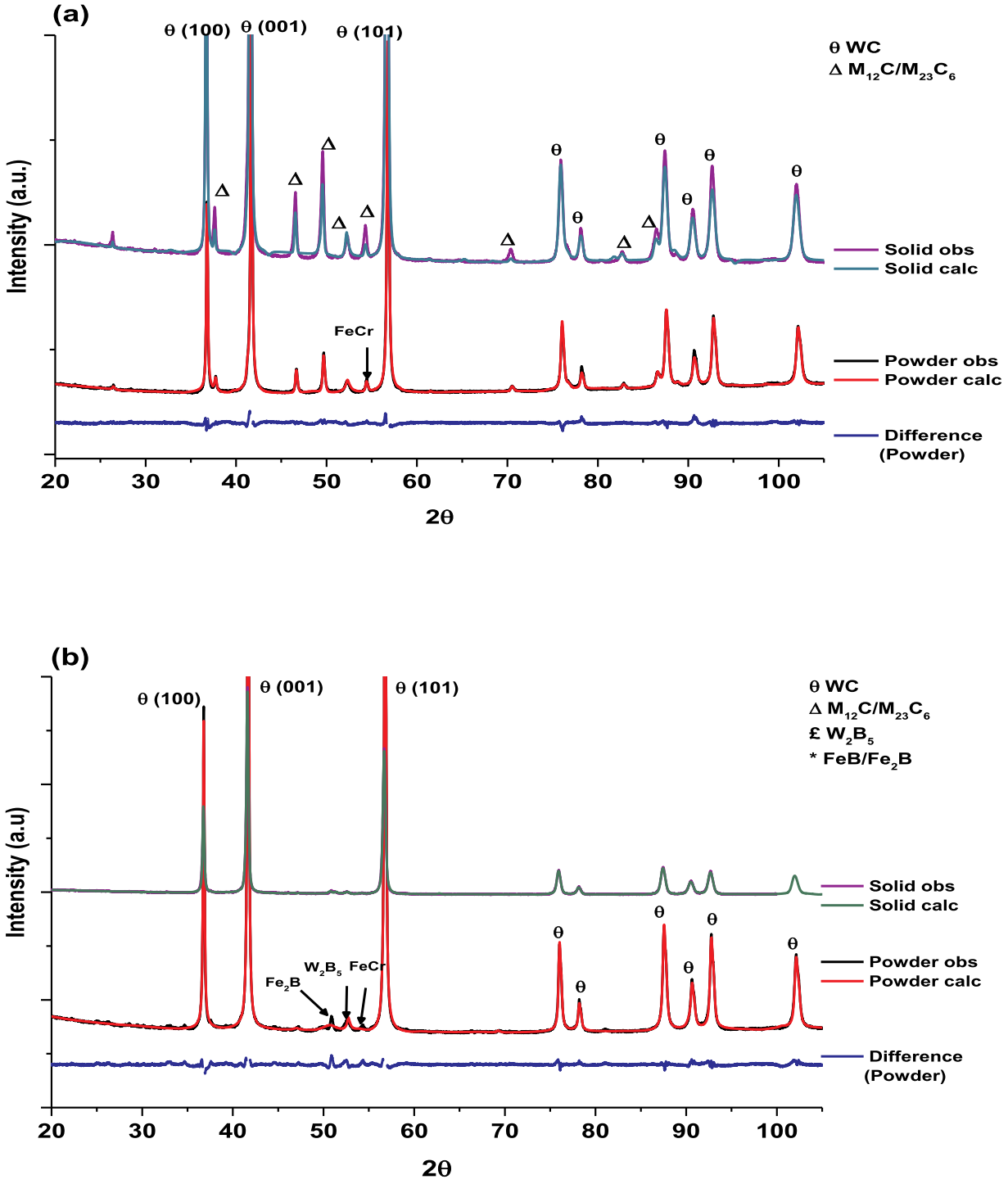

Fig. 4. XRD spectra from powder and solid cWC-RSB samples. (a) FeCr-cWC JBTE10, (b) Boron-doped FeCr-cWC B1TE10, (c) B4TE21W, (d) B5T522W, (e) B7TE23W and (f) B9TE25W. Peaks with 3 or more attributed phases were left unlabelled. For clarity, peaks from the solid patterns are only indexed where they differ from the powder patterns.

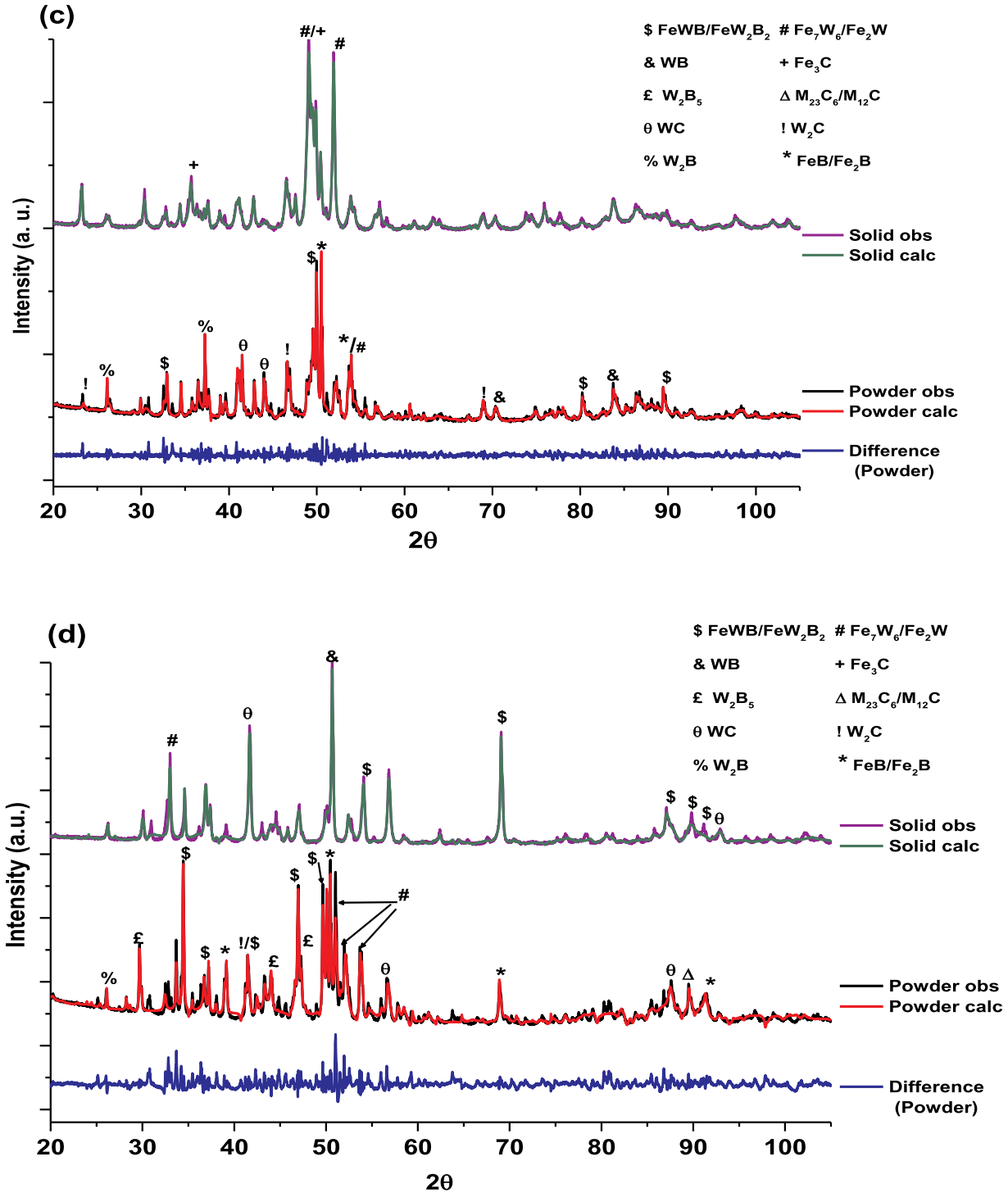

Fig. 4. (*continued*)

and a low R_{exp} makes for a rather high GOF, particularly for higher boron compositions. Factors that account for this are (1) underestimating standard errors, (2) model is incomplete or (3) model is systematically wrong [21]. (1) is possible but unlikely since the systematic error from the X-ray system is well understood and (3) is unlikely from the restraints used to eliminate models incompatible with sample chemistry. This leaves factor (2) in that there are almost certainly some missing phases as seen in the difference plots in Fig. 4(d)–(f). Another aspect for (2) is that if N is large (and R_{exp} is small), this magnifies minor imperfections when fitting.

Differences in at% between XRD models and ICP-EDX data for each atomic species with respect to powder compositions shown in the Supplementary Data. In general, XRD models for the cWC compositions JBTE10 and B1TE10 underestimate the Cr content, indicating that the $M_{12}C$ and $M_{23}C_6$ models are Cr-deficient compared to real phases. XRD models generally overestimated the boron content and underestimated carbon content in RSBs relative to EDX-ICP measurements, apart from composition B7TE23W where these trends are reversed. The presence of excess carbon relative to XRD models is indicative of free carbon present within the bulk of sintered RSBs. Alongside non-optimal PEG removal, free carbon presence indicates insufficient sintering time for carbide formation and other reactive species to go to completion for

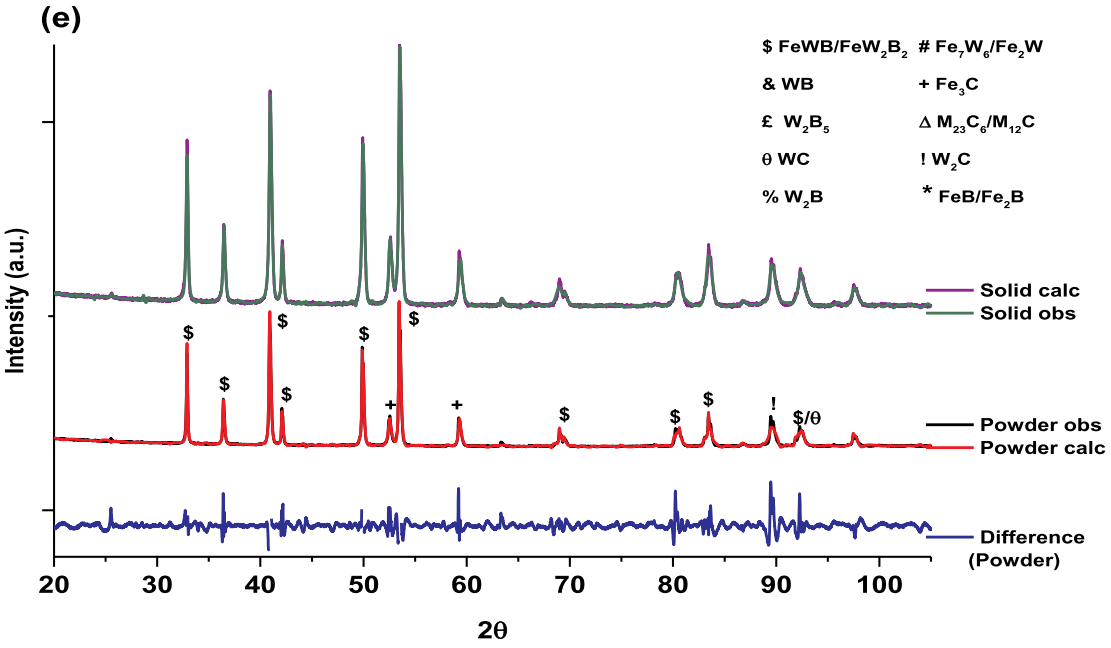

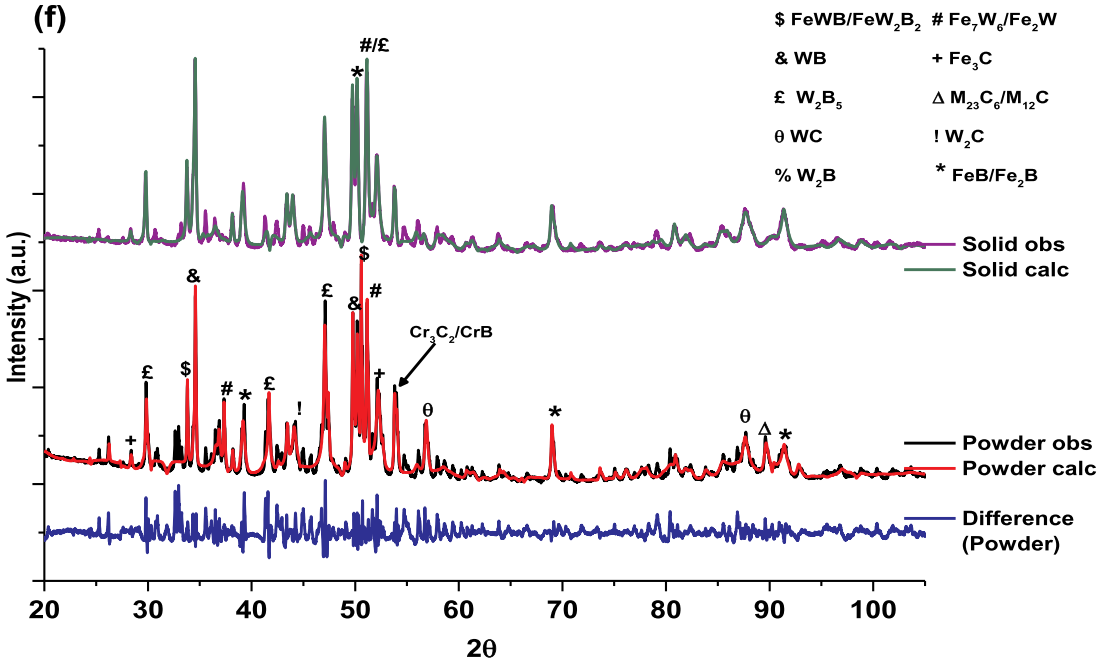

Fig. 4. (*continued*)

RSBs relative to cWCs. The presence of excess W in composition B4TE21W is more evidence that RSB compositions where starting B at% < 30% do not have sufficient boron (or carbon) to form a dense body on sintering since there is insufficient boron or carbon to form a stable, cohesive boro-carbide composite. While the models are arguably incomplete, they are of enough accuracy to enable a practical determination of theoretical densities for current RSB materials.

3.7. XRD density vs. Archimedes density

Theoretical densities of cWC and RSB materials were calculated from the weighted densities of indexed phases as determined from spectra shown in Fig. 4. Archimedes measurements were taken from a minimum of 4 discrete samples per composition of various geometries and compared with the calculated ρ_{XRD} derived from the TOPAS models with the lowest R_{wp} factors and closest convergence with ICP-EDX composition data. Archimedes and ρ_{XRD}-derived densities are shown in Table 4.

Both cWC compositions have low densities for 10 wt% binder compositions due to ternary phase presence $M_{12}C/M_{23}C_6$ and W_2B_5 for JBTE10 and B1TE10, respectively. Samples of compositions B4TE21W and B5T522W also had $\rho/\rho_{XRD} > 95\%$. While ρ/ρ_{XRD} might be high for composition B4TE21W, there is considerable evidence (Fig. 1(c), Table 2, Fig. 5) that this is a non-viable composition in its current form due to its brittleness and severe delamination on sintering. In contrast, B5T522W shows a density consistent with microstructural and

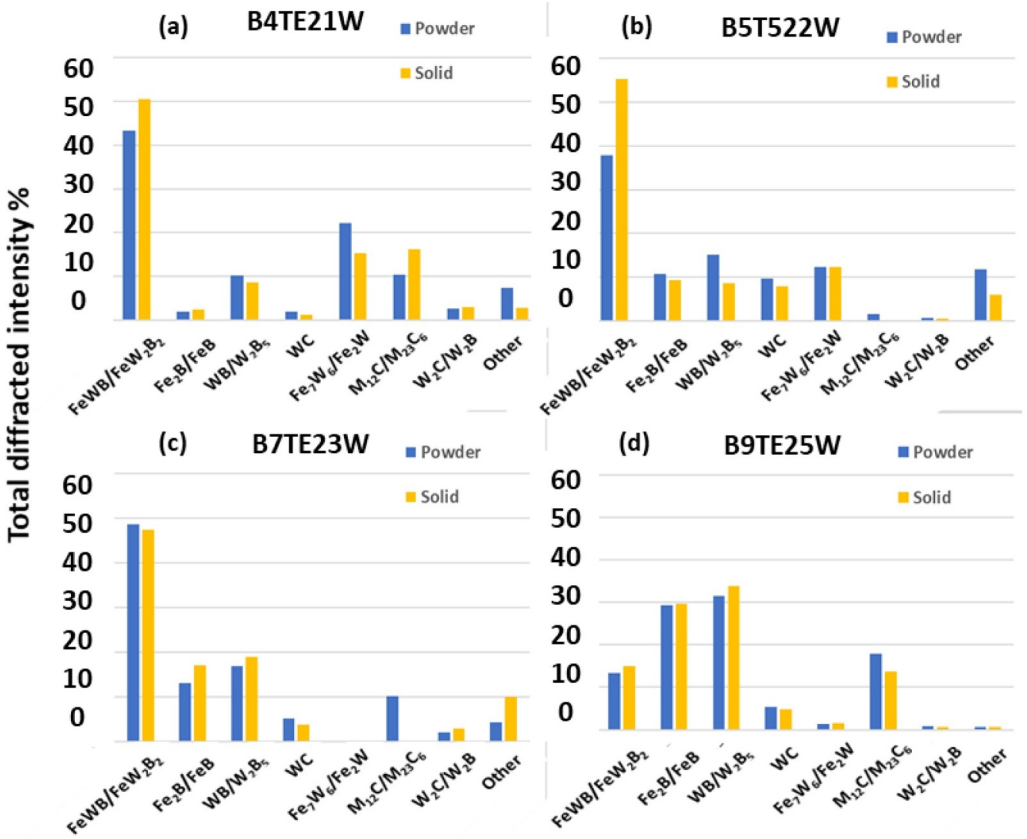

Fig. 5. Dominant phase abundance with increasing boron content for RSB compositions (a) B4TE21W, (b) B5T522W, (c) B7TE23W and (d) B9TE25W. Residual trace phases (Other) were mostly simple Cr and Fe carbides/borides.

Table 3
Bragg factors R_{wp}, R_{exp} and GOF for powder samples.

Composition	R_{wp}	R_{exp}	GoF R_{WP}/R_{exp}
JBTE10	1.657	0.526	3.148
B1TE10	1.286	0.491	2.616
B4TE21W	2.707	0.927	2.919
B5T522W	2.812	0.498	5.640
B7TE23W	3.053	0.511	5.968
B9TE25W	3.227	0.490	6.588

Table 4
Calculated and measured densities of cWC and boride compositions. Uncertainties are within the brackets, e.g. (13.06 ± 0.03) g cm^{-3}.

Composition	Measured ρ g cm^{-3}	ρ_{XRD} g cm^{-3}	ρ/ρ_{XRD} %
JBTE10	14.1(3)	14.5(2)	97.2
B1TE10	13.8(5)	14.4(1)	95.5
B4TE21W	12.7(5)	13.06(3)	97.2
B5T522W	12.5(1)	12.59(1)	99.3
B7TE23W	10.7(9)	12.27(4)	89.3
B9TE25W	10.3(3)	11.91(2)	87.2

mechanical testing and that any delamination features were few and widely spaced and present only in the wear test sample. B5T522W is the closest to optimal for an RSB composition when porosity and physical properties are considered. However, it must be noted that ρ_{XRD} calculated for composition B5T522W may not be the final optimized ρ_{XRD}, but it is probable that $\rho_{XRD,\ optimal} \approx 12.6$ g cm^{-3} for starting composition B5T522W.

The ρ/ρ_{XRD} ratios from B7TE23W and B9TE25W were considerably lower than for other compositions. This disparity is due to micro-porosity (Fig. 4(c)–(d)) but also from closed delamination features, revealed on cross-sections (Fig. 1(d)). As for B5T522W, some delamination features were not apparent until the sample was cut for cross-sectional analysis but unlike B5T522W, delamination features were present at all scales for compositions B7TE23W and B9TE25W. The combination of closed porosity and micro-delamination features would account for the sharp disparity in ρ/ρ_{XRD} seen in Table 4.

4. Conclusions

This study shows that despite their novelty, RSBs have development potential to be engineering materials compatible with PM processing and with applications including but not limited to shielding in highly irradiating environments. Solid RSBs with reasonable dimensional control and shrinkage were formed when B at% > 30 at% at the weigh-in. Composition B4TE21W where B at% = 25 at% at weigh-in formed brittle, distorted samples due to insufficient boro-carbide formation (Fig. 1(c)) and can be excluded as a candidate in its present form.

4.1. Sintering defects in RSBs

Out of all RSBs where B at% > 30 at%, the wear test samples of B5T522W had the fewest macroscopic defects, with some coarse delamination features on cross-sectioning. B7TE23W and B9TE25W samples had both fine and coarse delamination features down to microscopic dimensions, alongside the porosity observed in Fig. 3(e)–(f). Closed delamination and porosity are why compositions B7TE23W and B9TE25W have relatively low ρ/ρ_{XRD}, in Table 4. Compositions where B at% > 30% showed some evidence of converging towards sintered compositions where the atomic ratio for W: B: Fe ~ 1: 1: 1. This

indicates that for the W-B–Fe–Cr–C system, the composition closest to the pseudo-ternary W–B–Fe within this system at weigh-in will be the most stable with respect to porosity and delamination. The fact that only coarse delamination features were present in the wear test sample of B5T522W is indicative of this composition being closest to optimal out of all the RSB compositions even though the defect level for B5T522W is much greater than that of the cWC-based compositions JBTE10 and B1TE10. The first task of any subsequent work on RSB materials will be to establish the parameters needed for optimal PEG de-binding and sintering to ensure fully dense defect-free sintered bodies prior to any further thermo-mechanical testing relevant to reactor applications. These would include thermal conductivity and dilatometry as it is critical that candidate materials have rapid heat transfer and can maintain their dimensions at high temperatures over long times. It is anticipated that RSBs should have thermal conductivities similar to those of cWCs [1].

4.2. Microstructure and carbon content

Evidence of carbon-enrichment in the bulk relative to the surface in RSBs results partially from non-optimized PEG removal but also indicates incomplete carbon consumption since free carbon would not be present amongst Fe_xW_y intermetallics (Fig. 4) for materials closer to equilibrium. Carbide formation such as WC, $M_{12}C$ and Fe_3C would be expected to consume all carbon providing there was no carbon excess, but at this stage, it is unknown how much carbon is excessive as this would vary between specific RSB compositions. Carbon content was observed to have a significant role in the specific phase formation within RSB compositions even though micro-pores are associated with local carbon enrichment. Compositions B7TE23W and B9TE25W had similar atomic abundances post sintering but with significantly different microstructures. B7TE23W had more W and less C present post sintering relative to B9TE25W and was dominated by $FeWB/FeW_2B_2$ and FeB/Fe_2B (Figs. 3(e), (f) and 5). In contrast, B9TE25W was dominated by WB/W_2B_5 with significant WC presence, similar to B5T522W. WB/W_2B_5/WC phases are more evident in carbon-rich RSB composition and that $FeWB/FeW_2B_2/M_{12}C$ presence is more indicative of carbon-poor compositions.

4.3. Composition B5T522W – the candidate shielding RSB?

The composition closest to being optimal in terms of basic mechanical properties and density is composition B5T522W, the composition closest to the ternary W–B–Fe. system While baseline mechanical data can be obtained from the existing non-optimal B5T522W samples, fully dense samples of standard testing geometries will be required for comprehensive thermo-mechanical testing and other experimental work required to assess the suitability of cWC-RSB materials in realistic reactor settings, particularly with respect to thermal loading, cycling and extremes of temperatures (10–1000 K) that cWC-RSB materials must be able to provide mechanical and radiation integrity over the reactor lifetime. This will require further experiments to establish PEG de-binding cycles and optimal sintering conditions to ensure fully dense RSBs with no uncontrolled bulk-surface composition gradients. It is anticipated that even in optimized materials, composition B5T522W has a highly complex microstructure which has opportunities and threats when considering manufacture, thermal gradients and radiation response.

A recent study on He-implantation in Fe-Cr cWC [16] observed that bubble formed following He ion irradiation were considerably larger at WC/M_6C and WC/CrC_x interfaces than for WC/Fe-Cr and WC/WC interfaces – this has significant implications for the highly complex microstructure within B5T522W RSBs where there are numerous M_6C and mixed Cr-rich carbide regions (Figs. 4(d) and 5(d)). The presence, size and distribution of such carbide-rich regions will have important implications as to how any RSB will evolve with irradiation and thermal loading in a realistic reactor setting with respect to radiation-induced dislocations, ion implantation, creep and H/He production from transmutation, particularly from ^{10}B neutron absorption. Temperature (and hence part placement) is a particularly important aspect of how a B5T522W-based RSB part would be expected to evolve with time since temperature will govern the movement of dislocations and the growth of voids. This is a particular issue at cryogenic temperatures, since dislocation growth is much slower at low T and it is anticipated that void formation, He/H entrapment and swelling could be significantly worse at cryogenic temperatures near a superconducting magnet than those near the fuel side of a nuclear reactor (near the fissile material or plasma facing component for a fission or fusion reactor respectively). This is significant concerning RSB-based shielding solutions since the since the most probable placement for an early B5T522W-based neutron shield within a compact spherical tokamak reactor would be near the superconducting core [2,3].

Potential solutions to the issues resulting from radiation induced damage and gas formation are to use high surface area shielding designs incorporating cWC-RSB materials. A large surface area would enable dislocations to reach the surface and mitigate void formation to some extent, particularly at low T. Large surface area structures would enable rapid heat transfer from shielding to coolant, particularly at high temperatures which would be critical in managing the heat load generated during operation. Since cWC-RSB materials are produced by PM and extrusion techniques, it is not unreasonable to propose that large surface area structures and sheet extrusion would be feasible in an optimized RSB material alongside existing cWC extrusion once suitable process methods are established.

The partial raw data required to reproduce these findings are available to download https://wrap.warwick.ac.uk/128964. The processed data required to reproduce these findings are available to download from https://wrap.warwick.ac.uk/128964

CRediT authorship contribution statement

J.M. Marshall: Conceptualization, Methodology, Validation, Formal analysis, Resources, Writing - original draft, Writing - review & editing, Visualization, Supervision, Project administration, Funding acquisition. **D. Walker:** Formal analysis, Resources. **P.A. Thomas:** Resources, Supervision.

Declaration of Competing Interest

None.

Supplementary materials

Supplementary material associated with this article can be found, in the online version, at doi:10.1016/j.nme.2020.100732.

References

[1] S.A. Humphry-Baker, J.M. Marshall, G.D.W. Smith, W.E. Lee, Thermophysical properties of Co-free WC-FeCr hardmetals, Proceedings of the Nineteenth Plansee Seminar, 2017, pp. 1–13 http://wrap.warwick.ac.uk/94047.
[2] C.G. Windsor, J.M. Marshall, J.G. Morgan, J. Fair, G.D.W. Smith, A. Rajczyk-Wryk, J.M. Tarragó, Design of cemented tungsten carbide and boride-containing shields for a fusion power plant, Nucl. Fusion (2018) 58, https://doi.org/10.1088/1741-4326/aabdb0.
[3] C.G. Windsor, J.G. Morgan, P.F. Buxton, A.E. Costley, G.D.W. Smith, A. Sykes, Modelling the power deposition into a spherical tokamak fusion power plant, Nucl. Fusion 57 (2017) 036001, , https://doi.org/10.1088/1741-4326/57/3/036001.
[4] S.A. Humphry-Baker, G.D.W. Smith, Shielding materials in the compact spherical tokamak, Philos. Trans. R. Soc. A Math. Phys. Eng. Sci. (2019) 20170443, , https://doi.org/10.1098/rsta.2017.0443.
[5] S.A. Humphry-Baker, K. Peng, W.E. Lee, Oxidation resistant tungsten carbide hardmetals, Int. J. Refract. Met. Hard Mater. 66 (2017) 135–143, https://doi.org/10.1016/j.ijrmhm.2017.03.009.
[6] C. Daniel, The new shape of fusion, Science (80-.) 348 (2015) 854–856, https://doi.org/10.1126/science.348.6237.854.

[7] A.E. Costley, J. Hugill, P.F. Buxton, On the power and size of tokamak fusion pilot plants and reactors, Nucl. Fusion (2015) 55, https://doi.org/10.1088/0029-5515/55/3/033001.
[8] P. Bruzzone, W.H. Fietz, J.V. Minervini, M. Novikov, N. Yanagi, Y. Zhai, J. Zheng, High-Temperature superconductors (HTS) for fusion magnets, Nucl. Fusion (2018) 58, https://doi.org/10.1088/1741-4326/aad835.
[9] D.X. Fischer, R. Prokopec, J. Emhofer, M. Eisterer, The effect of fast neutron irradiation on the superconducting properties of REBCO coated conductors with and without artificial pinning centers, Supercond. Sci. Technol. 31 (2018) 44006, https://doi.org/10.1088/1361-6668/aaadf2.
[10] D. Hancock, D. Homfray, M. Porton, I. Todd, B. Wynne, Refractory metals as structural materials for fusion high heat flux components, J. Nucl. Mater. 512 (2018) 169–183, https://doi.org/10.1016/j.jnucmat.2018.09.052.
[11] H.L. Swami, C. Danani, A.K. Shaw, Activation characteristics of candidate structural materials for a near-term Indian fusion reactor and the impact of their impurities on design considerations, Plasma Sci. Technol. (2018) 20, https://doi.org/10.1088/2058-6272/aaabb4.
[12] S.C. Cifuentes, M.A. Monge, P. Pérez, On the oxidation mechanism of pure tungsten in the temperature range 600–800°C, Corros. Sci. 57 (2012) 114–121, https://doi.org/10.1016/j.corsci.2011.12.027.
[13] C.G. Windsor, J.G. Morgan, Neutron and gamma flux distributions and their implications for radiation damage in the shielded superconducting core of a fusion power plant, Nucl. Fusion (2017) 57, https://doi.org/10.1088/1741-4326/aa7e3e.
[14] J.M. Marshall, EP3401413A1 “An iron tungsten borocarbide body for nuclear shielding applications, (2018). doi:10.13140/RG.2.2.34460.13447.
[15] J.M. Marshall, EP3401414A1. Cemented carbides comprising a Fe–Cr binder metallic binder, (2019).
[16] S.A. Humphry-Baker, R.W. Harrison, G. Greaves, A.J. Knowles, G.D.W. Smith, S.E. Donnelly, W.E. Lee, A candidate fusion engineering material, WC-FeCr, Scr. Mater. 155 (2018) 129–133, https://doi.org/10.1016/j.scriptamat.2018.06.027.
[17] S. Humphry-Baker, J. Marshall, Structure and properties of high-hardness silicide coatings on cemented carbides for high-temperature applications, Coatings 8 (2018) 247, https://doi.org/10.3390/coatings8070247.
[18] X. Chong, Y. Jiang, R. Zhou, J. Feng, Stability, chemical bonding behavior, elastic properties and lattice thermal conductivity of molybdenum and tungsten borides under hydrostatic pressure, Ceram. Int. 42 (2016) 2117–2132, https://doi.org/10.1016/j.ceramint.2015.09.105.
[19] J.M. Marshall, M. Giraudel, The role of tungsten in the co binder: effects on WC grain size and hcp-fcc Co in the binder phase, Int. J. Refract. Met. Hard Mater. (2015) 49, https://doi.org/10.1016/j.ijrmhm.2014.09.028.
[20] J.M. Marshall, A. Kusoffsky, Binder phase structure in fine and coarse WC-Co hard metals with Cr and v carbide additions, Int. J. Refract. Met. Hard Mater. (2013) 40, https://doi.org/10.1016/j.ijrmhm.2013.04.001.
[21] B.H. Toby, R factors in Rietveld analysis: how good is good enough? Powder Diffr. 21 (2006) 67–70, https://doi.org/10.1154/1.2179804.
[22] R.A. Young, The Rietveld Method, 1995th ed., Oxford University Press, Oxford, 1993.
[23] G. Herranz, Control of carbon content in metal injection molding (MIM), Handb. Met. Inject. Mold. (2012) 265–304, https://doi.org/10.1533/9780857096234.2.265.
[24] All about cemented carbide, Hyperion Mater. Technol. (2019), http://www.allaboutcementedcarbide.com/.
[25] J. García, S. Englund, F. Haglöf, Controlling cobalt capping in sintering process of cermets, Int. J. Refract. Met. Hard Mater. 62 (2017) 126–133, https://doi.org/10.1016/j.ijrmhm.2016.06.008.
[26] J.J. Pittari, H.A. Murdoch, S.M. Kilczewski, B.C. Hornbuckle, J.J. Swab, K.A. Darling, J.C. Wright, Sintering of tungsten carbide cermets with an iron-based ternary alloy binder: processing and thermodynamic considerations, Int. J. Refract. Met. Hard Mater. 76 (2018) 1–11, https://doi.org/10.1016/j.ijrmhm.2018.05.008.
[27] A. Fernández Guillermet, The Co–Fe–Ni–W–C phase diagram: a thermodynamic description and calculated sections for (Co–Fe–Ni) bonded cemented Wc tools, Z. Met. 80 (1989) 83–94.